INT. J. REMOTE SENSING, 1993, VOL. 14, NO. 3, 425–440

SPOT multispectral data and digital terrain model for the analysis of ice-snow fields on arctic glaciers

J. F. PARROT
ORSTOM, 70 route d'Aulnay, 93140 Bondy, France and Université Paris IV

N. LYBERIS
Université Paris VI, D^{pt} de Geotectonique, 4 Place Jussieu, 75252 Paris Cedex 05, France

B. LEFAUCONNIER
Norsk Polaristitutt, Postboks 158, 1330 Oslo lufthavn, Norway

and G. MANBY
Thames Polytechnic, School of Earth Sciences, Walburgh House, Bigland Street, London, E1 2NG, U.K.

(Received 3 July 1990; in final form 13 July 1991)

Abstract. Satellite data from the Arctic present extensive shaded zones arising from the combination of low Sun elevation and mountainous topography. Field radiometry measurements from training zones on two glaciers in Arctic north-west Svalbard discriminate the different surface states of the glaciers. The SPOT reflectance values have been corrected using the slope orientation and dip parameters from the digital terrain model combined with the corresponding Sun elevation and azimuth. The reflectances of the shaded and illuminated zones have been restored to a new image based on the XS3 versus XS1 bimensional histogram. The pixel values of the new image can distinguish between firn and superimposed ice surface states on the glaciers defined and controlled by field measurements. From the new image a map of the different surface states of the glacier can be produced which is homogeneous in both the shaded and illuminated zones. The boundary between the firn and the superimposed ice can be located on the median and longitudinal profile of the glacier by combining the new image and the digital terrain model. With this method it is possible to locate the boundary between the firn and the superimposed ice and, consequently, the equilibrium line to within 40 m of altitude.

1. Introduction

The satellite-level radiance of a high spatial resolution snow-ice covered ground scene of sub-polar glaciers is affected by a number of factors including the Sun's position, atmospheric composition, reflectance of the region surrounding the scene and the terrain slope (Justice *et al.* 1981, Dave and Bernstein 1982). Justice and Holben (1979) have shown that the degree of the 'topographic effect' on sensor response varies considerably as a function of solar elevation. With the availability of

0143–1161/93 $10.00

multispectral data from SPOT satellites several studies have been undertaken aimed at the quantitative evaluation of the Sun's position and the topographic effects (e.g. Lyberis *et al.* 1990). The relations amongst the radiance recorded by the satellite sensors, the surface reflectance and the cosine of the solar zenith angle have been described by Wiscombe and Warren (1980), Choudhury and Chang (1981), Kowalik and Marsh (1982), and Lyberis *et al.* (1990).

The albedo contrast between the snow-ice fields and the rock outcrops is shown to be exaggerated by the satellite sensors. The albedos of the snow-ice fields are highest in the spectral bands sensed by the satellites and fall off rapidly in the near-infrared (Shine and Henderson-Sellers 1985). Consequently, the satellite records will tend to exaggerate the brightness of the snow and ice surfaces.

The aim of this paper is to show how the ice and snow fields of two sub-polar glaciers (figure 1) can be mapped, using SPOT satellite reflectances combined with digital terrain model (DTM) data (figure 2). The studied glaciers are formed by accumulation of successive layers of annually superimposed ice (Lliboutry 1965). The accumulation occurs mainly during the winter time and the ablation takes place during the summer time. At the end of the ablation period, the glacier surface is roughly divided into two areas with an accumulation zone on the upper part, and an ablation zone on the lower part. The equilibrium line (EL) corresponds to the boundary of those two parts and defines the position where the ablation (melting of ice and snow) is equal to the snow-ice accumulation.

The glacier surface presents, from the upper to the lower part, the firn zone, the firn line, the superimposed ice zone where the EL is located and the blue ice zone. Field radiometer measurements have been carried out in Brøggerbreen and Lovén-breen glaciers on training zones located in the field from the satellite images.

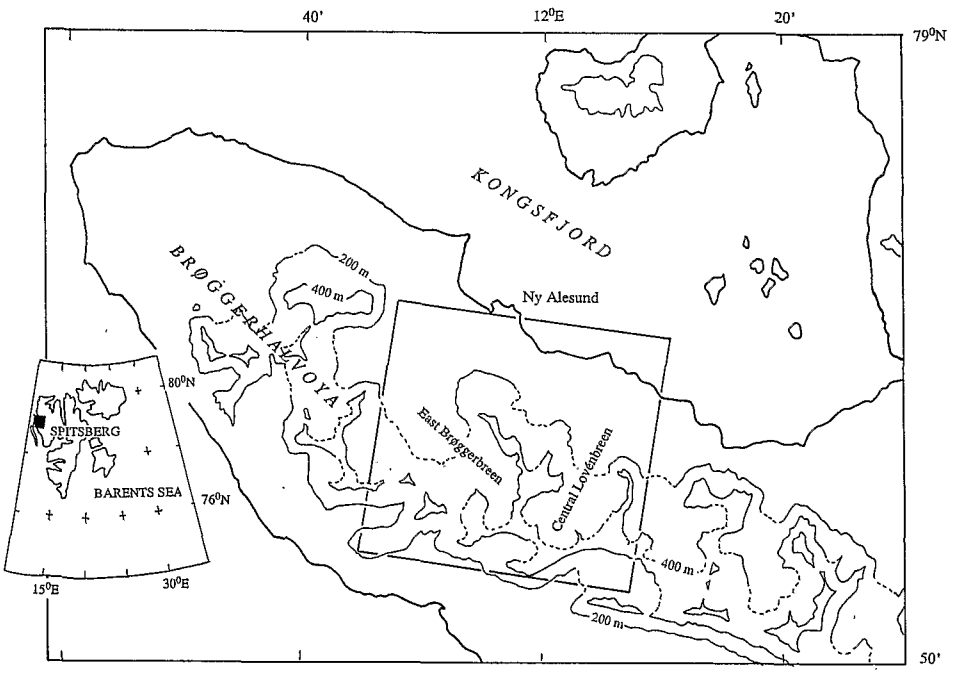

Figure 1. Position of the investigated area.

Reflectances calculated from the field measurements show that it is possible to distinguish the different surface states of the ice and snow fields of the studied glaciers. Fresh snow, settled snow, firn, superimposed ice and blue ice display pronounced reflectance differences in the 0·2–1·6 μm wavebands (Dozier 1984, Hall and Martinec 1985, Shine and Henderson-Sellers 1985, Dedieu and Elizechea 1988).

The method has been applied to two sub-polar glaciers in western Spitsbergen, At 79° N. East Brøggerbreen and Central Lovénbreen glaciers (figure 1) are situated on Brøggerhalvoya and lie between 50 and 600 m in altitude. They are northwards facing and they have a surface area of about 6 km^2.

The states of the glacier surface have been mapped using the results of the field measurements and the digital data of SPOT XS1, XS2 and XS3 bands. The processing developed here allocates the reflectance scale of the shaded zones to the scale of the reflectances of the illuminated zones. The method assigns the same value to a formation situated either in the shadow or in the illuminated zones and provides an homogeneous map of the glacier.

2. Satellite data

The available SPOT multispectral image ($k=152$, $j=140$, near nadir view angle) was acquired at 14 h 21 min GMT on 7 September 1986, when the Sun's elevation was 13·6° and the Sun's azimuth was 229·9°. The SPOT image used was taken after six sunny days.

The SPOT multispectral mode has three spectral bands (XS1, XS2 and XS3) in the visible and near-infrared wavelength ranges (0·50–0·59, 0·61–0·68 and 0·79–0·89 μm, respectively). The pixel size is 400 m^2 (20 m × 20 m). This scene is free of clouds and it was acquired in September at the end of the ice ablation period, three days before the first winter snow and cast shadows are predominant (figure 2).

The recorded albedo depends on the atmospheric conditions and the glacier surface properties. The spectral response of remotely sensed data partly depends on the radiance which is essentially a function of the slope, the Sun's azimuth and elevation angle (Holben and Justice 1980, 1981, Dave and Berstein 1982, Kowalik and Marsh 1982) and the structure of the ice and snow surfaces.

3. Field radiometer measurements

Some surface information is required to interpret remotely sensed data for environmental surveying, especially in the case of low-spectral resolution. Therefore, training zones have been defined as representative of the different ice and snow surfaces. They have been located on the satellite image in order to compare the field results and the satellite values. The field radiometer (CIMEL) measurements correspond to the ratio between the vertical component of the incident flux and the vertically reflected flux measured on a 1 m^2 surface. For each training zone, several measurements have been collected in 1987 and 1988 using the method described by Lyberis *et al.* (1990). Parameters such as albedo, information about the structure of the snow and the ice, the state of the surface, aspect of the site and inclination of the slope have been taken into account. Each set of measurements has been calibrated by comparison to a reference surface and restored on a homogeneous scale for the three SPOT bands (Lyberis *et al.* 1990).

Figure 3(*a*) integrates all the measurements obtained during two field seasons (August 1987 and August 1988) including those from clear and overcast sky conditions. The recorded values decrease from the fresh snow to the blue ice. A

(*a*)

(*b*)

dispersion, producing an important overlapping of the values, is observed for each surface state. Nevertheless, several general and significant trends are observed. First it is recognized that absorption coefficients of snow and ice are dependent on the ice-crystal size (Dozier *et al.* 1981) and the reflectance of snow and ice decreases with increasing crystal size (Hall and Martinec 1985, Sergent *et al.* 1987). At the end of the ablation period snow, firn and new superimposed ice have 2–5 mm crystal sizes whereas close to the front of the glacier, crystals of the blue ice up to 3 cm are predominent. Old snow induces a marked transparency carrying a reduction of the extinction coefficient in the visible and the near-infrared wavelengths (Chang *et al.* 1976, Wiscombe and Warren 1980, Sergent *et al.* 1987). In addition, the state of the surfaces changes during the ablation period when fresh snow is transformed into settled snow and firn corresponding to an increase of the crystal sizes.

The dispersion and the overlapping of the measured values of reflectance are due to the presence of dust which produces a reduction of the values in the three bands. Presence of water has the same effect, particularly in the third band (h, on figure 3(*b*)). Thus, clear blue ice is characterized by a higher value than dusty superimposed ice.

In addition, the weather conditions prior to the field radiometer measurements have to be taken into account because of changes in the state of the glacier surface. With sun and clear sky, glaciers receive far more solar than infrared radiation. A large part of the solar radiation penetrates the superficial layer of the ice producing a melting at the periphery of crystals and the ice bubbles. In addition, the evaporation is relatively high and the surface of the ice remains 'dry' increasing the ruggedness of the ice surface. In the three CIMEL bands the dynamic scale is then drastically reduced. On the other hands, when the sky is overcast, the received solar radiation decreases and the melting formerly described is weaker. Often the moisture maintains a film of water on the surface of the ice. Thus, this surface is smoother, the scattering is reduced and

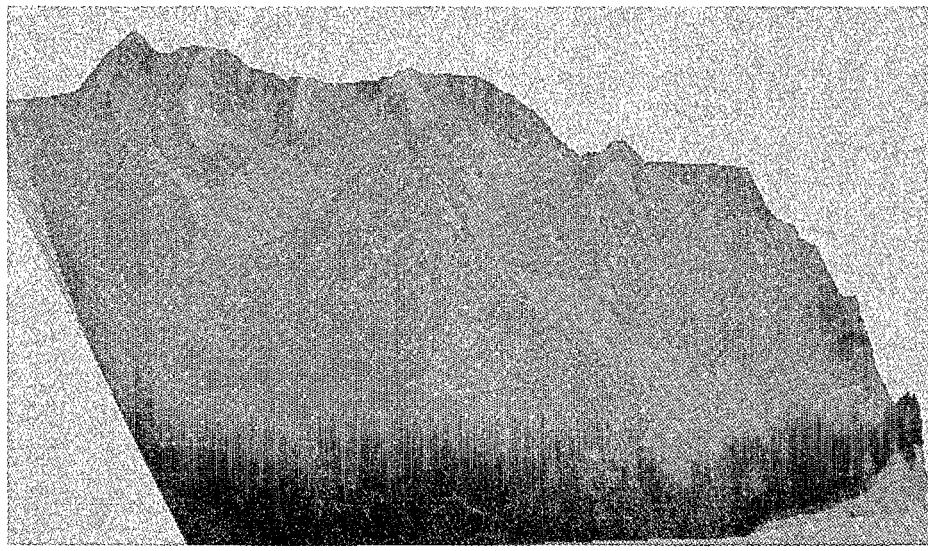

(*c*)

Figure 2. (*a*) SPOT-XS1 image of the studied glaciers, (*b*) SPOT-XS3 image of the studied glaciers, and (*c*) perspective view (XS3 superimposed on DTM), with 180° rotation.

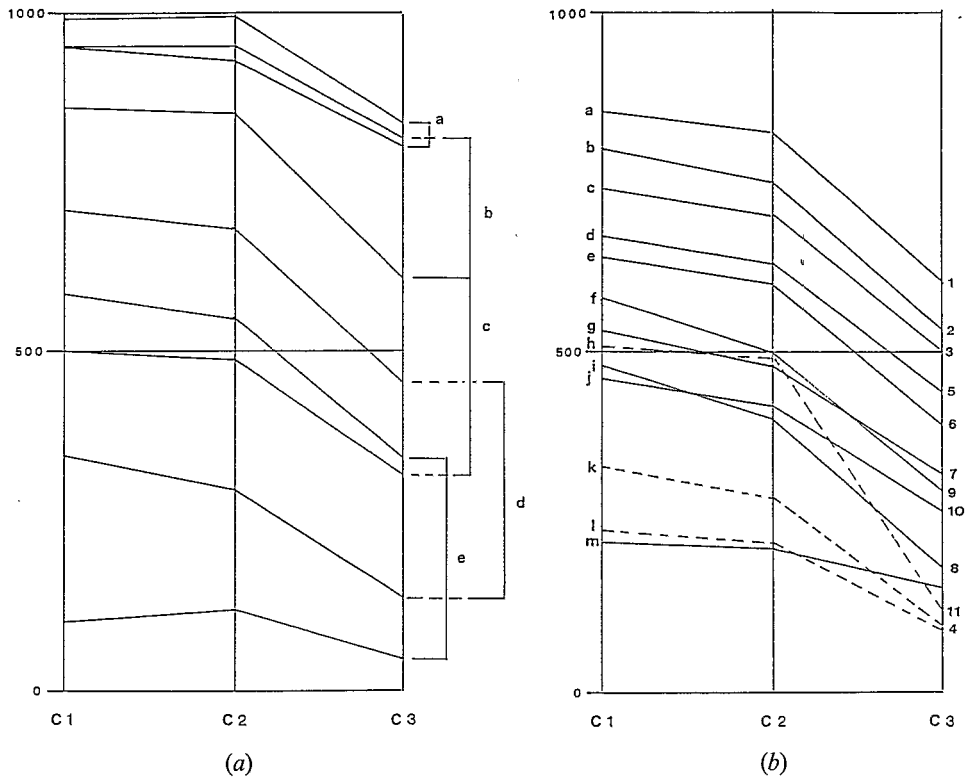

Figure 3. Reflectance measurements (August 1987 and 1988) on the three SPOT bands (C1, C2 and C3) obtained with a CIMEL radiometer. (*a*) Diagram showing the whole measurements. a, snow; b, settled snow; c. settled snow and firn; d, superimposed ice; e, blue ice. (*b*) Mean values obtained on 24 August 1988, along the central axis of the East Brogger glacier for chosen sites. The altitude decreases from 1 to 13. a, snow; b and c, firn; d and e, thick superimposed ice; f, blue ice; g, thin superimposed ice (<2 cm) on blue ice; h, superimposed ice covered by water; i. blue ice with some dust; j, blue ice, k, superimposed ice with slush and water; 1, superimposed ice with slush, water and dust; m, dirty blue ice.

the difference between the CIMEL values of snow and ice increases. Nevertheless, the dispersion is largely due to the multidate records and the overlapping of the CIMEL values is seriously reduced when the measurements are from the same day.

4. Topographic effects

The 'topographic effect' is manifested by the visual appearance of terrain ruggedness and is caused by the differential spectral radiance due to surface slope angle (Holben and Justice 1980, 1981). Holben and Justice (1981) proposed to correct the Landsat Multispectral Scanner (MSS) images for the topographic effect using a ratioing. Here, we propose to use the DTM for the calculation of the topographic effect on SPOT multispectral imagery. The 10 m contour lines have been digitized from the Norsk Polarinstitutt topographic maps of the Brøggerhalvoya peninsula (S10V28H60 and S10V28H55, 1/10 000, 1980 and 'Brøggerbreen Vestre og midre Lovénbreen', 1/20 000, 1979). The altitude of the points situated between these contour lines have been calculated by multidirectional linear interpolations.

The distributions of shadows calculated from the DTM is detailed below. For the investigated area, the slope direction, the dip and the variation of the dip (figure 6(*c*)) have been calculated from the DTM. On the basis of the distribution of the dip variation, the pixels over the whole scene have been recoded. Using the morphological recoding, we can identify the pixels which correspond to sharp crest, smooth crest, sharp thalweg, smooth thalweg, shoulder, convex and concave slope, flat surface, and a horizontal plane. The morphological recoding of the dip and the dip variations have to be combined with the satellite image.

The satellite radiometric values depend on the properties of the reflecting surface including the dip and the orientation of the slope. The natural surfaces are non-Lambertian but the nadir reflectance shows a decrease in error with decreasing solar zenith angle, from the hemispherical reflectance (Kimes and Kirchner 1982, Kimes and Sellers 1985). To simplify the calculation, and because of the lack of available information, it is assumed that the terrestral surfaces possess Lambertian properties in which case hemispherical reflectance is equal to the nadir reflectance. Therefore, the spectral irradiance (R) received at the sensor has to be corrected for the topographic effects taking into account the incident angle defined by the direction of the incident flux and the normal of the reflecting surface:

$$R = R_0 \times \cos\theta \tag{1}$$

$\cos\theta = \mathbf{n} \times \mathbf{s} / |\mathbf{n}| \times |\mathbf{s}|$ with

$$\mathbf{n} = \frac{1}{\sqrt{r^2 + \Delta x_x^2 + \Delta z_y^2}} \begin{bmatrix} \Delta z_x \\ -\Delta z_y \\ r \end{bmatrix} \quad \text{and} \quad \mathbf{s} = \begin{bmatrix} \cos(El) \times \sin(Az) \\ \cos(El) \times \cos(Az) \\ \sin(El) \end{bmatrix}$$

$$\cos\theta = \frac{\Delta z_x \times \cos(El) \times \sin(Az) - \Delta z_y \times \cos(El) \times \cos(Az) + r \times \sin(El)}{\sqrt{r^2 + \Delta z_x^2 + \Delta z_y^2}} \tag{2}$$

where θ is the angle between the incident flux and the normal of the ground surface, r is the distance between two successive points (20 m), Δz_x and Δz_y are the differences of altitude between two successive points on X and on Y, El is the Sun's elevation, Az is the Sun's azimuth, $\mathbf{n}$ is the normal to the ground surface, $\mathbf{s}$ is the incident flux and R is the reflected flux after correction for the topography. The negative sign of the y component is due to the raster-scan order, that is row–column order from top left to lower right.

A new image has been obtained by replacing the value R_0 recorded from the satellite, by the calculated value R. The following process has been applied on the new images R of the three SPOT bands. Atmospheric effects, emphasized by Singh and Cracknell (1985) are not addressed here. However, these effects are less important for the Spitsbergen latitude, with clear sky, because of the high atmospheric optical depth.

5. Reflectance scales on shaded and illuminated zones

The discrimination of the different superficial formations of the glaciers is based on the equilibration of the spectral responses both in the illuminated and shaded zones. Two methods, taking into account the DTM, have been used.

5.1. *Distribution of the shadow on the DTM*

The first method consists of obtaining a map (x', y') showing the distribution of the shadow on the DTM at the time that the scene was acquired (Figure 4). The

method used to calculate the illumination is based on an elementary model. On the hoizontal plane (x, y), for each pixel (i, j), the altitude $(z_{i,j})$ combined with the altitude of the two neighbouring pixels $(i, j+1; i+1, j)$, define a surface whose the normal is calculated. The reflection on a reflecting mirror is described by Lambert's law and the flux reflected is proportional to the cosine of the angle θ, defined by the direction of the incident flux and the normal of the reflecting surfaces (equation (3)).

$$l = l_i \times kd \times \cos\theta \tag{3}$$

with $0 < \theta < \pi/2$, if not:

$$l = 0$$

where, l is reflected flux, l_i is incident flux, and k_d is the diffusion coefficient.

Equation (3) gives the distribution of the shadow. The pixels of the shaded zones are recoded with 0 and the pixels corresponding to the cast shadow are determined

Figure 4. Shadow distribution calculated from the DTM for a Sun azimuth and elevation corresponding to the available SPOT image.

by equation (4). The whole scene is scanned, in the x direction and in the y direction, to define the pixels S (x_s, z_s) corresponding to the crest lines. The illumination of the pixels is calculated by taking into account their altitude and their position with regard to the neighbouring crest lines. For a scanning following x, the position of the illuminated pixels is given by

$$x_s+\alpha x_v=x_j+\delta(x_{j+1}-x_j)$$
$$z_s+\alpha z_v=z_j+\delta(z_{j+1}-z_j) \tag{4}$$

When $\alpha>0$ and $0<\delta<1$ the corresponding pixel is located out of the cast shadow produced by the last crest point and the direction of the solar flux (x_v, z_v) at the point S. If not, the corresponding pixel of the x', y' plane is recoded with 0. When $\alpha>0$ and $0<\delta<1$, the reflected flux 1, given by equation (1) for each illuminated pixel of the DTM surface, is projected orthogonally on an horizontal plane (x', y'). This processing is repeated for the y direction.

This simulation of the shadow extension from the DTM, for a given Sun azimuth and elevation, does not take into account the diffuse flux which is present in the shaded zones. This approach however does not distinguish the shadow from the cast shadow which are recoded with the same value (figure 4).

5.2. *Rectification of the SPOT reflectances using the DTM*

The SPOT digital numbers (ID(i, j)) of the shaded zones and those of the illuminated zones have been processed separately. The whole digital numbers of the two zones have been restored on the dynamic scale (0, 255) using the values (TD(i, j)) of the illuminated DTM. The restored values (RR) have been calculated in order to obtain a simulation of the original SPOT image on an horizontal surface.

In this approach we have assumed that the ID and their corresponding maximum TD values are described by a straight line. This line corresponds to a theoretical maximum of a homogeneous surface which is dependent on the illumination angle, without any correction for saturation and absorption.

The restored values RR, in the shady zones are given by

$$\mathrm{RR}=[\mathrm{ID}(i,j)/\mathrm{TD}(i,j)]\lambda\cot\alpha \tag{5}$$

and in the illuminated zones, are given by

$$\mathrm{RR}=[(\mathrm{ID}(i,j)-S_t)/(\mathrm{TD}(i,j)-S_d]\lambda\cot\beta \tag{6}$$

where i is the line number, j is the column number, $\lambda=255$, S_t SPOT digital value of the shadow–light boundary, S_d is the value of the shadow–light boundary on the illuminated DTM, α is the angle between the regressive line and the TD (i, j) axis for the values of the shady zones, and β is the angle between the regressive line and the ID (i, j) axis for the values of the illuminated zones.

Equation (5) cannot be applied when the shadow and the cast shadow are recoded with the same value, because in this case $\alpha=90°$. The projection of the RR values on a horizontal plane (equation (6)) can be used only for the illuminated zones. Therefore, the linear stretching of the reflectances from the shaded zones is not sufficient to erase the topographic effects. However, if the shaded zones are masked and recoded to zero on the illuminated DTM, the reflectance values of the shadow zone, can be determined in the three SPOT bands. The values obtained by this method for the boundaries between the shaded and illuminated zones in the

different SPOT bands are used in the following treatment where the altitude of the EL on the glaciers is defined on the DTM.

5.3. *Bidimensional histogram*

The equilibration of the reflectances in the shaded and the illuminated zones can be explored using the XS1 and XS3 SPOT bands which shows the least degree of correlation. The spectral responses depend on Sun and view geometry and their effect is more pronounced for the highly absorptive red (0·6–0·7 mm) and near-infrared wavelength band (Ranson *et al.* 1985).

The bidimensional histogram XS3 band versus XS1 band presents two different trends (figure 5(*a*)). In the first trend, the values of XS3 are relatively low and correspond to the ice and snow domain. The second trend is characterized by the weak values of XS1 and stretched values on XS3. This second trend corresponds to neighbouring rock outcrops. The shadow–light boundary defined by the comparison of the DTM and the SPOT data is reported on the bimensional histogram XS3 versus XS1 (figure 5(*a*)).

The distribution of the pixels on the bidimensional histogram presents a clear limit between the two trends, characterized by relatively low values. The points of the bidimensional histogram corresponding to a number of pixels less than 100 are scattered and they have been eliminated.

Using the bidimensional histogram, a similar dynamic scale for the shaded and the illuminated zones is obtained (figure 6(*a*) and 6(*b*)). The surrounding rock units have not been considered in this processing. The ice and snow fields of the shaded zones have been separated from the ice and snow fields situated in the illuminated zones. Each field can be described by a regression line with an envelope (figure 5(*b*)). The regression line (bc) corresponding to the illuminated zone is a continuation of that for the shaded zone (ab). The transition between shadow and light corresponds to the point b. Each point of the shaded zone is projected on the regression line (ab) and each point of the illuminated zone is projected on (bc). In this process the points on the regression line are projected orthogonally and the calculated values are stretched to obtain the new channel NC which is calibrated 0–200 (Delaune and Parrot, 1993). The equation ($y=Az+B$) of the regression line (ab) is calculated (equation (7)).

$$A=(\mathrm{XS1(b)}-\mathrm{XS1(a)})/(\mathrm{XS3(b)}-\mathrm{XS3(a)})$$
$$B=\mathrm{XS1(a)}-(A\times\mathrm{XS3(a)}) \tag{7}$$

where XS1(a) and XS3(a) are the coordinates on the bidimentional histogram XS1/XS3 of the point (a), XS1(b) and XS3(b) are the coordinates of the point (b).

If a pixel (i, j) corresponds, on the bidimensional histogram XS1/XS3, to a point d(XS1(i, j), XS3(i, j)), the equation ($y=A'x+B'$) of the line perpendicular to the regression line (ab) issued from a point d contained in the envelope, is

$$A'=-1/A$$
$$B'=\mathrm{XS1(d}(i,j))-(A'\times\mathrm{XS3(d}(i,j))) \tag{8}$$

The coordinates $d'(i, j)$ of the intersection between ($y=Ax+B$) and ($y=A'x+B'$) are

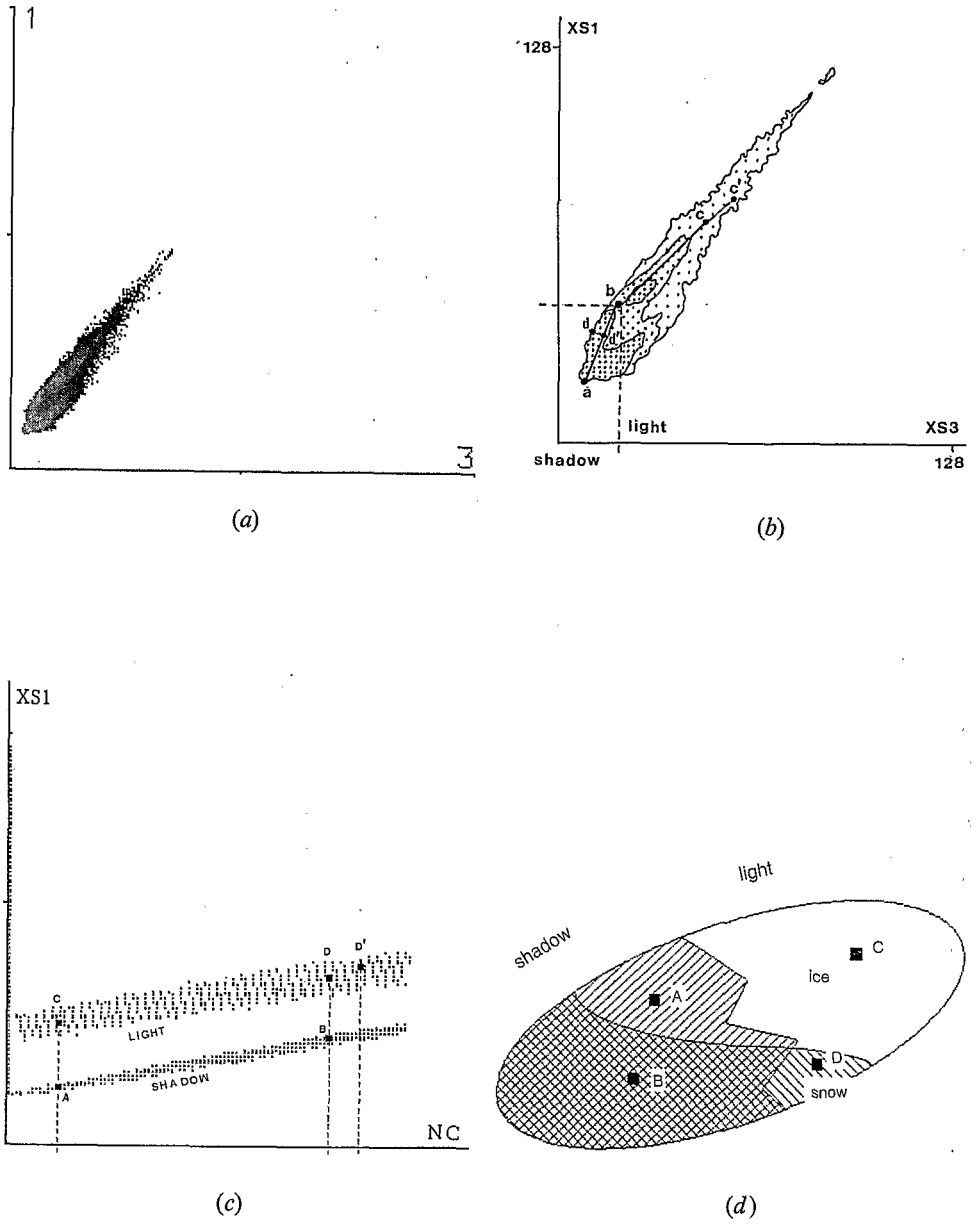

Figure 5. (*a*) Bidimensional histogram XS1 versus XS3, (*b*) Sketch showing the main trends of the bidimensional histogram XS1/XS3. ab, regression line for the shaded zone; bc, regression line for the illuminated zone; c′, recalculated position of the point c. (*c*) Bidimensional histogram XS1 versus NC. A, B, C and D, training zones of the figure 5(*d*). D′, recalculated position of the point D. (*d*) Sketch showing four training zones. A and C, corresponds to ice, B and D, corresponds to show. A and B are located in the shaded zones, C and D are located in the illuminated zones.

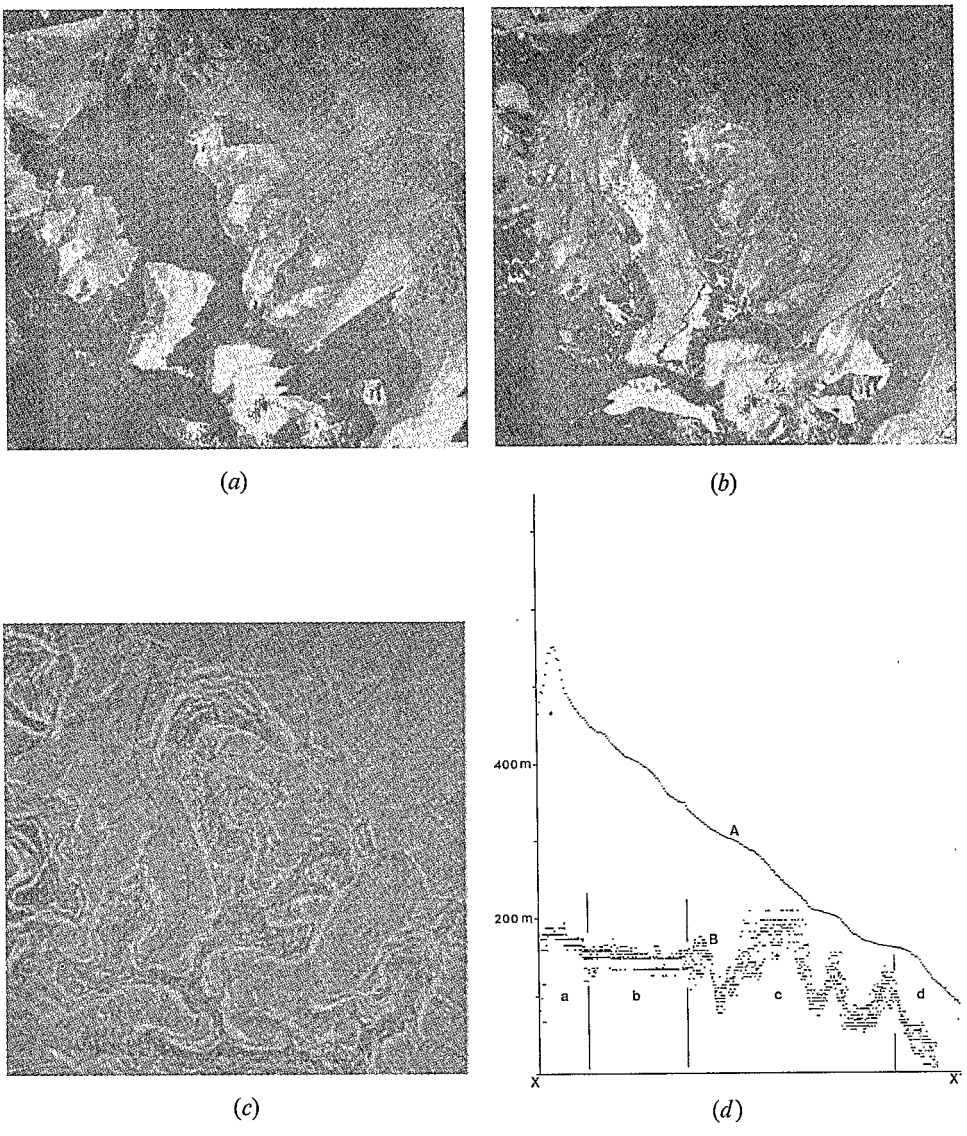

Figure 6. (*a*) The shaded parts of the studied image (figure 2(*a*) and 2(*b*)) recoded on the 0–200 dynamic scale. (*b*) Image of the investigated glaciers without shadow. The limit between shaded and illuminated zones is plotted on the glacier surface. (*c*) Dip variations calculated from the DTM (thick line, location of the profile reported on figure 6(*d*)). (*d*) Median and longitudinal topographic profile of the Brøggerbreen glacier (A) and corresponding NC values (B). a, firn situated up to 460 m; b, superimposed ice located between 460 and 340 m; c, particular surface conditions; d, regular decreasing.

$$x=(B'-B)/(A-A')$$

$$y=Ax+B \text{ or } y=A'x+B'$$

The value of the pixel (i, j) of the NC1 is:

$$\mathrm{NC1}(i,j)=(\mathrm{ad'/ab})\times S) \tag{9}$$

where $S=200$; and NC1 is the neochannel for the shaded zone.

The same calculation is applied for the illuminated zones (NC2). Using this method two neochannels were obtained corresponding to the snow and ice fields in the shaded and illuminated zones, respectively. First, the dynamism of the two ice and snow fields in the two neochannels was considered to be equivalent to one another. The addition of the two neochannels (NC1 and NC2) produces a third one (NC), also calibrated 0–200, on which the ice and snow fields do not present any discontinuity arising from the illumination.

The bidimensional histogram XS1/NC (or XS3/NC) exhibits two trends corresponding to the shaded and the illuminated zones (figure 5(*c*)). The information provided by the field measurements is used at this stage to correct, if required, the coordinates of point (c) on the bidimensional histogram XS1/XS3 (end of the regression line of the light field, figure 5(*b*)). The maximum and the minimum values recorded in the XS3 band have been chosen to represent the illuminated and shaded areas in the training zones.

The method of recalculation can be illustrated by reference to figure 5(*c*). Two examples are given, one from an ice field, the other from a snow field and both span the shaded–illuminated zones boundary. In figure 5(*d*) training zone A from the shaded part of the ice field corresponds, on the histogram XS3 versus NC, to training zone C in the illuminated part of the same ice field. Similarly, training zone B, which is located in the shaded part of the snow field, corresponds to training zone D in the illuminated part. Figure 5(*c*) illustrates the positions of the training zones A, B, C and D on the bidimensional histogram XS3 versus NC. If any difference between the two similar training zones (A, B and C, D) on the axis NC of the bidimensional histogram XS3/NC is observed the length of the regression line (b) it is corrected in such a way that the point (c) is located in (c′) (figure 5(*c*)).

Thus, by analysing the distribution of the recalculated reflectances it is possible to obtain an image free of shadow and in which any discontinuity between the illuminated and shaded zones is erased (figure 6(*b*)).

6. Characteristics of the glaciers surface on the NC band

In the whole scene, the reflectances of the glacier surface, in the shaded and the illuminated zones, gradually decrease from the top to the bottom. The difference in the reflectances (DR) between the neighbouring pixels (calculated from a multidirectional histogram of the differences between the reflectance values of two contiguous pixels) is generally 1–2, following the direction of the dip of the glacier. Only at the shadow–light limit is an important break of reflectances observed. High DR values are produced by water flow on the glacier and by the rock–glacier boundary (figure 6(*b*)). The gradual increase in the reflectances does not permit the definition of the ice and snow limits by simple thresholding based on the multidirectional histogram of their differences.

On the NC band of the two investigated glaciers it is possible to locate the EL, defined by field survey (Hagen and Liestøl 1987). Descriptive statistics have been done on the neochannel NC, for well-defined training zones, corresponding to the permanent markers of the glaciological survey, including the EL area. The blue ice, firn and other surface states of the glacier can be discriminated in the NC band but, because of the wide range of NC values encountered along the EL, no significant break corresponding to the EL is observed. In the NC band the values for the EL zone are wider than expected. The vague spectral characteristics of the EL zone are due to its unique location on sub-polar glaciers. The EL of the Spitsbergen glaciers

does not correspond to the firn–ice boundary, as observed in alpine glaciers where the EL is located close to this limit (Reynaud *et al.* 1984). On sub-polar glaciers, the EL is situated downwards from the firn line (lower limit of the firn), because of the presence of superimposed ice. This superimposed ice is formed by either refreezing of melt water during the autumn and/or during the ablation period, or refreezing of melt water on the glacier surface, below the firn line at the end of the ablation period. The position of the EL does not always coincide with the boundary between the superimposed and blue ice but it is located above this boundary. Thus, it is difficult to distinguish in the field the latest ice layer from the previous ones and the distinction is similarly difficult on the satellite images. However, the method developed here would be applicable to glaciers in temperate areas.

7. Comparison between the NC band and the DTM

The differences between firn, superimposed ice and blue ice on the NC band are weak and their limits do not present significant reflectance breaks. This is partly due, in both glaciers, to the position of the drainage basin with respect to the Sun's azimuth on both shady and illuminated zones and the results should be improved by an analysis of several glaciers with different surface orientation. However, the principal characteristics of the glacier surfaces can be identified on the NC band along a median–longitudinal profile.

Figure 6(*d*) shows the median and longitudinal topographic profile of the Brøggerbreen glacier (A) and the corresponding NC values calculated on a five-pixels wide strip (B). The NC profile shows four zones: a, an area of the highest NC values, situated up to a height of 460 m; b, a plateau of NC values corresponding to 460–340 m altitude; c, serrated NC values due to particular surface conditions such as dust accumulations, running water, etc.; d, a zone of regularly decreasing NC values toward the front of the glacier. However, field observations have shown that at 460–340 m altitude the Brøggerbreen glacier is characterized by homogeneous reflectance values. This area is covered by superimposed ice formed at the end of the ablation period. The boundaries of the b area should be used for the mapping of the limit between firn and superimposed ice.

8. Discussion and conclusion

A method is presented of analysis of the sub-polar glaciers based on the DTM which provided the shadow extension with respect to the Sun's azimuth and elevation. The DTM is used for a first correction of the satellite gross values according to the illumination angle and to define the limit between shaded and illuminated areas. The corrected reflectances of the shady and the illuminated zones have been restored to a common spectrum (255) on a new image (NC) by using of the bidimensional histogram XS3 versus XS1. This image corresponds to homogeneous glacier surfaces which do not present any discontinuity when crossing the original light–shadow limit.

In the two glaciers studied, the EL is situated in the superimposed ice zone. Thus, it is difficult to distinguish the latest ice layer from previous layers, both in the field and on satellite images. The annual displacement of the EL is related to the evolution of the mass balance which is directly linked to the climate (Martin 1977, Lefauconnier and Hagen 1990). Therefore, the climatological evolution of this area could be determined by annually monitoring the position of the Equilibrium Line from satellite data (Østrem 1975). On the basis of data accumulated over 20 years,

significant correlations between mass balances and altitude of the EL have been calculated for the two glaciers investigated in this study (Hagen and Liestøl 1987). The correlation coefficients are 0·95 and 0·92 for the Brøggerbreen (Brogger glacier) and the Lovénbreen (Loven glacier), respectively.

Whilst it is not yet possible to locate precisely the EL for sub-polar glaciers, the boundary between the firn and the superimposed ice can be identified on the new images. This boundary has been located for the Brøggerbreen and Lovénbreen on longitudinal profiles on the NC band and confirmed by field measurements on the surface states of the glaciers. Because the EL lies within the firn-superimposed ice boundary its position can be estimated, following the method described here, to within 40 m altitude.

Acknowledgments

The authors wish to express our special thanks to Professor Michel Durand for continued support of our research efforts. Financial support provided by the ATP-TELEDECTION project of CNRS as well as by the French–Norwegian Research Foundation. The fieldwork benefitted from logistic support by the Norsk Polarinstitutt.

References

CHANG, T. C., GLOERSEN, P., SCHMUGGE, T., WILHEIT, T. T., and ZWALLY, H. J., 1976, Microwave emission from snow and glacier ice. *Journal of Glaciology*, **16**, 23–39.

CHOUDHURY, B., and CHANG, T. C., 1981, On the angular variation of solar reflectance of snow. *Jounal of Geophisical Research*, **86**, 465–472.

DAVE, J. V., and BERNSTEIN, R., 1982, Effect of terrain orientation and solar position on satellite-level luminance observations. *Remote Sensing of Environment*, **12**, 331–348.

DEDIEU, J. P., and ELIZECHEA, E., 1988, Surveillance satellitaire des surfaces englacées et enneigées dans les Alpes Françaises par mesure de reflectances visibles et proche infrarouge issues des capteurs SPOT et Landsat Thematic Mapper. In *Proc. 4th International Colloquium on Spectral Signatures of Objects in Remote Sensing*, pp. 371–375.

DELAUNE, M., and PARROT, J. F., 1993, Large scale lithologic mapping *International Journal of Remote Sensing*, in press.

DOZIER, J., 1984, Snow reflectance from Landsat-4 Thematic Mapper. *IEEE Transactions on Geoscience and Remote Sensing*, **GE-22**, 323–328.

DOZIER, J., SCHNEIDER, S. R., and MCGINNIS, JR., D. F., 1981, Effect of grain size and snowpack water equivalence on visible and near-infrared satellite observations of snow. *Water Resources Research*, **17**, 1213–1221.

HAGEN, J. O., and Leistøl, O., 1987, Glacier mass balances investigations in the balance years 1984–1985 and 1985–1986. *Polar Research*, **5**, 2.

HALL, D. K., and MARTINEC, J., 1985, *Remote Sensing of Ice and Snow*. Chapman and Hall.

HOLBEN, B. N., and JUSTICE, C. O., 1980, The topographic effect on the spectral response of nadir-pointing sensors. *Photogrammetric Engineering and Remote Sensing*, **46**, 1191–1199.

HOLBEN, B. N., and JUSTICE, C. O., 1981, An examination of spectral band ratioing to reduce the topographic effect on remotely sensed data. *International Journal of Remote Sensing*, **2**, 115–133.

JUSTICE, C. O., and HOLBEN, B. N., 1979, Examination of Lambertian and non-Lambertian models for simulating the topographic effect on remotely sensed data. NASA TM 80557. (Greenbelt, MD: Goddard Space Flight Center).

JUSTICE, C. O., WHARTON, S. W., and HOLBEN, B. N., 1981, Application of digital terrain data to qualify and reduce the topographic effect on Landsat data. *International Journal of Remote Sensing*, **2**, 213–230.

KIMES, D. S., and KIRCHNER, J. A., 1982, Irradiance measurement errors due to the assumption of a Lambertian reference panel. *Remote Sensing and Environment*, **12,** 141–149.

KIMES, D. S., and SELLERS, P. J., 1985, Inferring hemispherical reflectance of the Earth's surface for global energy budgets from remotely sensed nadir or directional radiance values. *Remote Sensing and Environment*, **18,** 205–223.

KOWALIK, W. S., and MARSH, S. E., 1982, A relation between Landsat digital numbers, surface reflectance, and the cosine of the solar zenith angle. *Remote Sensing and Environment*, **12,** 39–55.

LEFAUCONNIER, B., and HAGEN, J. O., 1990, Glaciers and climate in Svalbard, statistical analysis and reconstruction of the Brogger glacier mass balance for the last 77 years. *Symposium on Ice and Climate, IGS Seattle, 21–25 August 1989, Annals of Glaciology,* **14,** 148–152.

LLIBOUTRY, L., 1965, *Traité de Glaciologie*, Tome 1, v. I, (Paris: Masson), 427 p.

LYBERIS, N., PARROT, J.-F., CHOROWICZ, J., and RUDANT, J.-P., 1990, Geological features of the Spitsbergen region obtained from Multispectral SPOT data and field radiometer measurements. *International Journal of Remote Sensing*, **11,** 253–265.

MARTIN, S., 1977, Analyse et reconstruction de la série de bilans annuels du Glacier de Sarenne. *Zeitschrift für Gletscherkunde und Glazialgeologie*, **13,** 125–163.

ØSTREM, G., 1975, ERTS data in glaciology—an effort to monitor glacier mass balance from satellite imagery. *Journal of Glaciology*, **15,** 403–415.

REYNAUD, L., VALLON, M., and LETREGUILLY, A., 1984, Spatio-temporal distribution of the glacial mass balance in the Alpine, Scandinavian and Tien shan areas. *Geograpfisca Annaler*, **66,** 239–247.

SERGENT, C., CHEVRAND, P., LAFEUILLE, J., and MARBOUTY, D., 1987, Caractérisation optique de différents types de neige, extinction de la lumière dans la neige. *Journal de Physique,* **48,** 361–367.

SHINE, K. P., and HENDERSON-SELLERS, A., 1985, The influence of satellite spectral sensor response on the analysis of satellite imagery at high latitudes. *International Journal of Remote Sensing*, **6,** 29–34.

SINGH, S. M., and CRACKNELL, A. P., 1985, The estimation of atmospheric effects for SPOT using AVHRR channel-1 data. *International Journal of Remote Sensing*, **7,** 361–377.

WISCOMBE, W. J., and WARREN, S. G., 1980, 1980, A model for the spectral albedo of snow, 2, Snow containing atmospheric aerosols. *Journal of Atmospheric Science*, **37**, 2712–2744.